Optical Materials: X 21 (2024) 100288

Contents lists available at ScienceDirect

Optical Materials: X

journal homepage: www.journals.elsevier.com/optical-materials-x

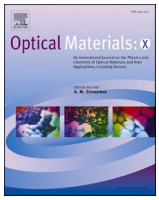

Photoluminescence and X-ray induced scintillation in Gd^{3+}-Tb^{3+} co-doped fluoride-phosphate glasses, and derived glass-ceramics containing $NaGdF_4$ nanocrystals

Gustavo Galleani [a,b,*], Thiago A. Lodi [a], Robin L. Conner [c], Luiz G. Jacobsohn [c,**,1], Andrea S. S. de Camargo [a,d,e]

[a] São Carlos Institute of Physics, University of São Carlos, São Carlos, SP, Brazil
[b] FunGlass, Alexander Dubček University of Trenčín, Študentská 2, SK-911 50, Trenčín, Slovakia
[c] Department of Materials Science and Engineering, Clemson University, Clemson, SC, USA
[d] Federal Institute of Materials Research and Testing (BAM), Berlin, Germany
[e] Otto Schott Institute of Materials Research, Friedrich Schiller University, Jena, Germany

A B S T R A C T

The glass system ($50NaPO_3$–$20BaF_2$–$10CaF_2$–$20GdF_3$)-x$TbCl_3$ with x = 0.3, 1, 3, 5, and 10 wt % was investigated. We successfully produced transparent glass ceramic (GC) scintillators with x = 1 through a melt-quenching process followed by thermal treatment. The luminescence and crystallization characteristics of these materials were thoroughly examined using various analytical methods. The nanocrystallization of Tb^{3+}-doped $Na_5Gd_9F_{32}$ within the doped fluoride-phosphate glasses resulted in enhanced photoluminescence (PL) and radioluminescence (RL) of the Tb^{3+} ions. The GC exhibited an internal PL quantum yield of 33 % and the integrated RL intensity across the UV-visible range was 36 % of that reported for the commercial BGO powder scintillator. This research showcases that Tb-doped fluoride-phosphate GCs containing nanocrystalline $Na_5Gd_9F_{32}$ have the potential to serve as efficient scintillators while having lower melting temperature compared to traditional silicate and germanate glasses.

1. Introduction

Scintillators are materials that convert the energy of charged particles (e.g., α and β) and high-energy photons (X-rays, γ-rays) into multiple lower-energy photons within the visible and ultraviolet (UV) range. Photodetectors like photodiodes (PD) and photomultiplier tubes (PMTs) detect these photons, allowing the use of these sensors in diverse applications such as industrial and medical imaging, homeland security, and high-energy physics experiments [1].

Common scintillators are traditionally based on crystalline inorganic materials such as CsI [2], Gd_2O_2S:Pr,Ce,F [3], $LaBr_3$:Ce [4], $Lu_3Al_5O_{12}$:Ce [5], NaI:Tl [6], $Bi_4Ge_3O_{12}$ [7] and $Y_3Al_5O_{12}$:Ce [8]. Although efficient in detecting ionizing radiation, these crystals can be hygroscopic, costly and challenging to manufacture with precise composition and uniformity, potentially limiting their widespread accessibility and usage in certain applications. Besides inorganic single crystals, transparent ceramics [9,10], glasses [11–18], nanoparticles [19,20] and polymers [21] loaded with scintillating compounds have also been proposed as scintillators. These materials are mostly doped with rare-earth elements, such as Ce^{3+}, Tb^{3+}, Eu^{3+} and others [22–24] due to their unique luminescent properties. The dopants can enhance light output, improve energy resolution, and tailor the emission spectrum of the scintillator to match the compatibility with the detector.

Among the diverse forms of scintillators, glasses are attractive considering their cost-effectiveness, large-scale production capabilities, large compositional range and the possibility to be processed into complex geometries, including optical fibers. However, glasses have numerous defects responsible for non-radiative recombination, which, in turn, are responsible for low light yields [25].

To overcome the issue of low light yields of glasses, a promising new class of inorganic scintillators that is cost-effective and has excellent optical properties for detecting high-energy photons was proposed: the luminescent glass-ceramics (GCs) [26,27]. Luminescent GCs compose an emerging class of photonic materials in which luminescent nanocrystals

* Corresponding author. São Carlos Institute of Physics, University of São Carlos, São Carlos, SP, Brazil.
** Corresponding author.
E-mail addresses: gustavo.galleani@tnuni.sk (G. Galleani), luiz@g.clemson.edu (L.G. Jacobsohn).
[1] Given his role as Editor of this journal, Luiz G. Jacobsohn had no involvement in the peer-review of articles for which he was an author and had no access to information regarding their peer-review. Full responsibility for the peer-review process for this article was delegated to another Editor.

https://doi.org/10.1016/j.omx.2023.100288
Received 9 October 2023; Received in revised form 1 December 2023; Accepted 11 December 2023
Available online 17 December 2023

are uniformly dispersed in the amorphous glass matrix. There has been growing interest in the use of GCs as scintillators, firstly based on transparent oxide glasses hosting the precipitation of traditional scintillation crystals [28,29].

At first, typical inorganic halide crystals, including alkali-earth halides and alkali-metal halides such as, CaI_2 [30], SrI_2 [31], $BaCl_2$ [32], $BaBr_2$ [32], BaI_2 [32], etc., and lately various oxyfluoride GCs matrix systems [26,27,29,33,34] have been proposed as GCs scintillators. Among them, the precipitation of different low-phonon fluoride nanocrystals has been targeted, including GdF_3 [33], $BaGdF_5$ [35], $BaYF_5$ [36], $BaLuF_5$ [37] and KLu_2F_7 [28]. These GCs showed that the X-ray excited luminescence was greatly enhanced in the oxyfluoride glass after the precipitation of the respective fluoride crystals. However, the low fraction of halide nanocrystals in the glass host limited the light yield of the final material. Furthermore, common oxide glasses have a high melting temperature (above 1300 °C) [38] causing high volatilization of the aimed halides to be precipitated, as well as limited solubility, leading to GCs with lower efficiency.

Therefore, to overcome these issues, mixed fluorophosphate glass networks have garnered substantial interest for applications that need high light yield [39–41]. Fluoride phosphate glass networks combine the best properties of phosphate glasses and fluoride glasses, i.e. lower phonon energy fluoride crystals precipitated in an oxide glass matrix with higher mechanical strength, chemical durability and thermal stability. In these networks, the efficient dispersion of luminescent species and high amount of fluoride lead to higher fraction of precipitated crystals. Also, the ordered nature of the crystalline phases in glass-ceramics are expected to lead to more efficient energy transfer to the luminescent centers and a higher probability of radiative recombination. For a given combination of glass and nanocrystalline phase, when the nanocrystals are significantly smaller than the wavelength of the emitted light, reduced light scattering results in higher transparency [42]. Despite these advantages, few studies have been done on the scintillation applications of these materials.

GCs scintillators have become particularly interesting for medical applications, for instance, as panels in X-ray imaging and recoverable X-ray storage plates. They are potential candidates to replace conventional silver-halide based panels, being an ideal low-cost solution with relatively high quantum yield. The addition of isotopes such as ^6Li and ^{10}B to these GCs has shown to render high sensitivity to thermal neutrons [43,44], opening the perspective of use as neutron scintillators. Therefore, the development of GCs scintillators, especially those based on mixed fluoride phosphate glass matrices that can potentially precipitate high fractions of fluoride crystals are of particularly interest. Further advantages include matrices that can be melted below 1000 °C with high chemical and mechanical stability and flexible applications.

These characteristics are necessary but not sufficient for obtaining a GC scintillator material with potential use in commercial applications [27].An essential factor that influences the quality of a scintillator is the selection of rare-earth dopants, responsible for the luminescence when exposed to ionizing radiation. Among the RE ions that present 4f-4f transitions in the UV–visible detection window of commercial detectors such as PMTs, Tb^{3+} shows the strongest emission in the green. Other ions such as gadolinium (Gd^{3+}) can play the role as a sensitizer, transferring the energy absorbed by the material to the luminescent Tb^{3+} centers.

In this work, a mixed fluorophosphate glass system with low melting temperature when compared to common oxide glasses and containing a high fluoride concentration was prepared and characterized. The glasses were prepared by the melt quenching technique and subjected to further thermal treatment that led to the formation of $Na_5Gd_9F_{32}$ nanocrystals within the fluoride-phosphate glass network. The energy transfer mechanism from Gd^{3+} to Tb^{3+} ions in fluoride-phosphate glasses and glass-ceramics containing $NaGdF_4$ nanocrystals was probed through excitation with UV light and X-rays and the influence of the precipitation of fluoride nanocrystals on the luminescent properties was evaluated.

2. Experimental procedure

2.1. Bulk glass synthesis

Glass samples in the system ($50NaPO_3$–$20BaF_2$–$10CaF_2$–$20GdF_3$)-$xTbCl_3$ with variable terbium (Tb) content (x = 0, 0.3, 1, 3, 5, and 10 wt %) were produced using the conventional melt-quenching technique. The glasses were labeled as follow: NPGF_xTb, with x being the $TbCl_3$ wt. % in the glass composition and NPGF for the undoped glass (x = 0). The precursor raw materials included $NaPO_3$, CaF_2, BaF_2, $TbCl_3$, and GdF_3. The GdF_3 precursor was prepared according to our previous work [45], involving the heating of Gd_2O_3 with an excess of ammonium bifluoride ($NH_4H_2F_3$). Since terbium can take chemical states +3 and + 4, the use of $TbCl_3$ was an attempt to achieve Tb^{3+}, luminescent in the green. All components were carefully weighed, mixed, and melted to produce bulk samples with 15g.

2.2. Fluoride-phosphate GCs preparation

Previously selected glass pieces were carefully heated within a defined temperature range bracketed by their glass transition temperature (*Tg*) and crystallization temperature (*Tx*) (Tg = 290 °C and Tx = 380 °C) [46] to ascertain the ideal temperature for nanocrystals precipitation within the glass matrix. In this study, a straightforward method was employed to determine the optimal temperature using a trial-and-error process. We conducted thermal treatments on bulky glass pieces for a fixed duration of 1 h at various temperatures. The temperature at which visible volume crystallization occurred in the glass volume was determined as the optimal temperature, which was found to be 340 °C. Following this, polished NPGF_1 Tb glass pieces were subjected to heat treatment at 340 °C for different durations (from 30 min to 6 h). This method ensured reproducibility across different parent glasses of the same composition. The GCs were labeled according to the duration of heat treatment at 340 °C of the glass sample NPGF_1 Tb as follow: GC_30min, GC_2 h and GC_6 h.

2.3. Glass sample characterization

Optical absorption spectra were obtained using a Cary 500 double-beam spectrometer within the wavelength range from 200 to 600 nm employing polished samples of approximately 2 mm thickness. X-ray diffraction (XRD) measurements were conducted using the powder diffraction method at room temperature, after grinding the parent glass and GCs that underwent heat treatment at 340 °C for 2–6 h. The GCs microstructure were examined using a JEM-2100-JEOL transmission electron microscope operating at 80 kV. The samples were first crushed in ethanol and a drop of the solution with small nanocrystals in suspension was deposited onto a carbon coated copper grid.

Photoluminescence excitation (PLE) and emission (PL) spectra in the visible range were measured using a Horiba Jobin Yvon Fluorolog spectrofluorometer model FL3-221. The excitation was performed using a continuous wave (CW) lamp at 273 nm to access Gd^{3+} transitions and the emission spectra were recorded, particularly in the range of Tb^{3+} main emission at 542 nm. Luminescence decay curves of Gd^{3+} and Tb^{3+} were measured using a pulsed Xe lamp under excitation at 273 nm and analyzed using a double monochromator configuration.

RL measurements were recorded using a Freiberg Instruments Lexsyg Research spectrofluorometer equipped with a Varian Medical Systems VF50J X-ray tube operating at 40 kV and 1 mA, coupled with a spectrograph and a CCD camera.

3. Results and discussion

3.1. Tb^{3+} doped fluoride-phosphate glasses

The absorption spectrum for the representative NPGF_1 Tb glass

sample within the 250–600 nm spectral range is illustrated in Fig. 1. The absorption bands associated with Gd^{3+} are distinctly observed at 245, 251, 273, 305, and 312 nm, corresponding to transitions from the ground state $^8S_{7/2}$ to the excited states ^6G_j, ^6D_j, ^6I_j, and ^6P_J, respectively [47]. Furthermore, a characteristic absorption band at 380 nm, corresponds to the $^7F_6 \rightarrow ^5D_3$ transition of Tb^{3+} [48].

Fig. 2 illustrates the excitation spectra of NPGF_*x*Tb glasses, measured by monitoring the green emission of Tb^{3+} ions at 542 nm (Tb^{3+}: $^5D_4 \rightarrow ^7F_5$). In these spectra, multiple peaks are noticeable in the near UV range at 245 nm, 272 nm, 305 nm, and 311 nm, attributed to Gd^{3+} transitions: $^8S_{7/2} \rightarrow ^6D_{9/2}$, ^6I_J, $^6P_{7/2}$, and $^6P_{5/2}$, respectively. Additionally, peaks at 278 nm and 284 nm are ascribed to the Tb^{3+} transitions $^7F_6 \rightarrow ^5H_6$ and $^3H_6$, respectively. Moreover, a broad band spanning from 240 to 265 nm is observed and attributed to the $4f^{(8)} \rightarrow 4f^{(7)}5d$ spin-allowed inter-configurational Tb^{3+} transition [13].

Above 300 nm, aside from the Gd^{3+} absorption bands, seven distinct bands corresponding to Tb^{3+} intra-4f transitions are observed. The presence of the Gd^{3+} transitions evidences the $Gd^{3+} \rightarrow Tb^{3+}$ energy transfer which is responsible for the increased emission intensity observed under UV or X-ray excitation of Tb^{3+} in glasses containing Gd^{3+}, as extensively reported in the literature [49–51].

The PL spectra of NPGF:Tb^{3+} glasses were measured with excitation at 350 nm (Tb^{3+}: $^7F_6 \rightarrow ^5D_3$) and at 273 nm (Gd^{3+}: $^8S_{7/2} \rightarrow ^6I_j$) within the range of 400–700 nm and are presented in Fig. 3(a) and (b), respectively. The luminescent behavior and potential $Gd^{3+} \rightarrow Tb^{3+}$ energy transfer (ET) processes are emphasized. For the 273 nm excitation, the spectra were normalized to the 311 nm band associated with the Gd^{3+}: $^8S_{3/2} \rightarrow ^6P_{7/2}$ transition.

Upon excitation at 273 nm (Fig. 3a), a single narrow emission band corresponding to the Gd^{3+}: $^8S_{3/2} \rightarrow ^6P_{7/2}$ transition at 311 nm is observed for the undoped NPGF glass. Upon the addition of Tb^{3+} ions, additional bands originating from the $^5D_4$ and $^5D_3$ excited levels of Tb^{3+} ions appear at 412, 435, 456, and 472 nm (Tb^{3+}: $^5D_3 \rightarrow ^7F_5$, $^7F_4$, $^7F_3$, $^7F_2$ transitions), as well as at 489 and 544 nm (Tb^{3+}: $^5D_4 \rightarrow ^7F_6$, $^7F_5$ transitions). Despite the consistent presence of Gd^{3+}, the emission at 311 nm significantly decreases with the incorporation of Tb^{3+} ions in the glass (inset of Fig. 3a). Concurrently, there is an enhancement of Tb^{3+} emissions relative to the Gd^{3+} emission. This observation reinforces the existence of energy transfer from Gd^{3+} to Tb^{3+} ions. Gd^{3+} electrons are excited from the $^8S_{7/2}$ state to the ^6I_j state and then relax to the $^6P_{7/2}$ state. As this state is at a higher energy than the $^5D_4$ level of Tb^{3+} ions, energy can be partially transferred to the latter, resulting in emissions from the $^5D_4$ level as the system returns to the ground state [51].

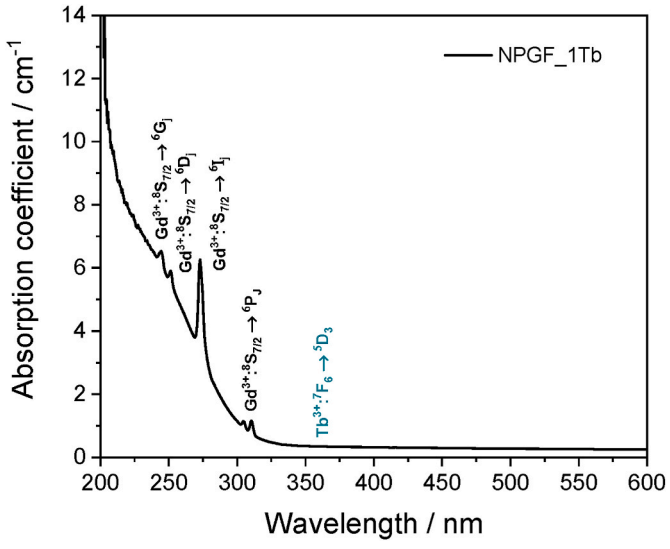

Fig. 1. Representative absorption spectrum obtained for the NPGF_1 Tb glass.

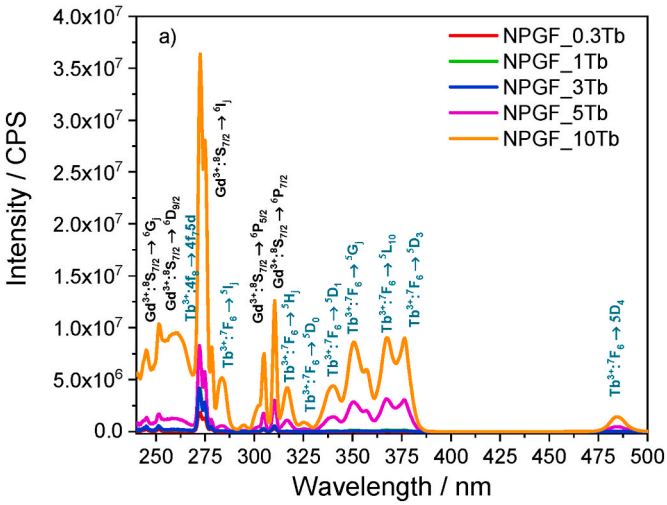

Fig. 2. Excitation spectra of NPGF glasses with different Tb^{3+} content, λ_{em} = 542 nm.

The changes in fluorescence intensity from $^5D_3$ to $^5D_4$ observed in the inset of Fig. 3a and better visualized by directly excitation of Tb^{3+} ions at 350 nm (Fig. 3b) result from the cross-relaxation mechanism (CR, Tb^{3+}: $^5D_3 + ^7F_0 \rightarrow ^5D_4 + ^7F_6$) [52], a phenomenon extensively documented in the literature for Tb^{3+} doped glasses [13,53]. This is because the energy gap between these levels is remarkably similar. Both energy transfer processes ($Gd^{3+} \rightarrow Tb^{3+}$ and CR, Tb^{3+}: $^5D_3 + ^7F_0 \rightarrow ^5D_4 + ^7F_6$) appear to exist in the studied glasses. The augmentation of emission from the $^5D_4$ level of Tb^{3+} is particularly beneficial for aligning emission wavelengths with the camera's optimal quantum efficiency spectral region (typically, 450–600 nm for PMTs) used in scintillators. The green emission of Tb^{3+} ions ($^5D_4 \rightarrow ^7F_5$ transition) appear to be the most intense in our glasses.

To further explore the emission characteristics of the glasses, we measured the internal PL quantum yield (QY), defined as the ratio of emitted photons (N_{em}) to absorbed photons (N_{abs}), for the emission at 549 nm. We conducted these measurements using an integrating sphere for the NPGF_03 Tb and NPGF_10 Tb samples, obtaining QY values of 16 % and 50 %, respectively, which is comparable to the values reported in the literature for other glass scintillators [54,55].

To validate the energy transfer (ET) process between Gd^{3+} and Tb^{3+} ions, we utilized fluorescence decay analysis (see Fig. 4a). By analyzing the luminescence decay curves corresponding to the Gd^{3+}: $^8S_{3/2} \rightarrow ^6P_{7/2}$ transition at 311 nm after excitation at 273 nm, both in the absence and presence of Tb^{3+}, we observed a decrease in the effective lifetime values of $^8S_{3/2}$. Moreover, the decay became strongly non-exponential due to additional depopulation paths from the cited emitter level, reducing the effective lifetime from 8.0 ms (NPGF) to 0.16 ms (NPGF_10 Tb). These results validate the occurrence of energy transfer from the $^8S_{3/2}$ level of Gd^{3+} ions to the neighboring Tb^{3+} ions.

In Fig. 4b, the luminescence decay curves detected at 541 nm (Tb^{3+}: $^5D_4 \rightarrow ^7F_5$) are presented. These curves were precisely fitted using a single exponential function for samples with all doping concentrations. As the Tb^{3+} content increases, the lifetime values slight decreases from 4.3 ms to 3.8 ms for NPGF_0.3 Tb and NPGF_10 Tb, respectively. This reduction is due to a higher population of Tb^{3+}:$^5D_4$ level, increasing the probability of CR and energy migration between ions.

X-ray-induced scintillation spectra are depicted in Fig. 5. Within these spectra, the emissions from the Tb-doped glasses are prominently characterized by the green emission of Tb^{3+} at 541 nm (Tb^{3+}: $^5D_4 \rightarrow ^7F_5$). Concurrently, emission from Gd^{3+} at 311 nm is also observed. As the Tb^{3+} ion content in the glasses increases, there is a notable augmentation in the overall emission intensity of Tb^{3+}, as also observed after excitation with UV light, despite the excitation mechanisms involved being different. Remarkably, the glass sample with a Tb^{3+} level of 10

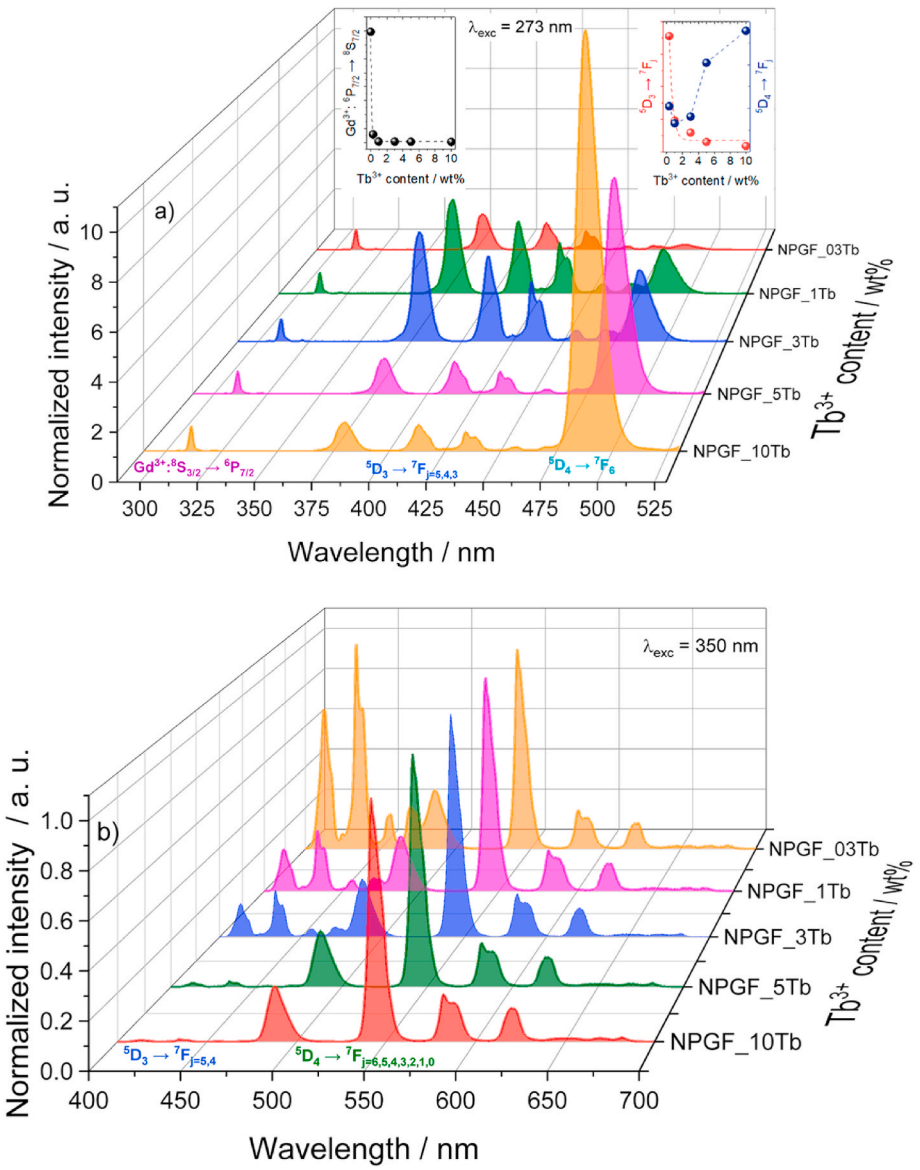

Fig. 3. Normalized photoluminescence emission spectra: (a) with excitation at 273 nm (Gd^{3+}: $^8S_{7/2} \rightarrow {}^6I_j$), spectra are normalized by the Gd^{3+}: $^8S_{3/2} \rightarrow {}^6P_{7/2}$ transition, and (b) at 350 nm (Tb^{3+}: $^7F_6 \rightarrow {}^5H_7$), spectra are normalized by the Tb^{3+}: $^5D_4 \rightarrow {}^7F_5$ transition. Inset: Integrated areas of Gd^{3+}: $^8P_{7/2} \rightarrow {}^8S_{7/2}$ (black circles), Tb^{3+}: $^5D_3 \rightarrow {}^7F_j = 5–3$ (red circles) and Tb^{3+}: $^5D_4 \rightarrow {}^7F_6$ (blue circles) transitions as a function of Tb^{3+} content. (For interpretation of the references to colour in this figure legend, the reader is referred to the Web version of this article.)

mol% exhibits the highest scintillation intensity emission, and there is no evidence of concentration quenching.

3.2. Tb^{3+} doped fluoride-phosphate glass-ceramics

In a subsequent step, GCs were prepared using the NPGF_1 Tb sample as a proof of concept. The objective was to analyze the influence of nanocrystallization of fluorides in the glass matrix, aiming at enhanced luminescence emission towards practical application as scintillators.

The transmission spectra measured at various heat-treatment times for the NPGF_1 Tb glass ceramics and the accompanying photograph, taken under daylight, are provided in Fig. 6. As evident from both the spectra and the photograph of the glass-ceramics, transparency decreases with increasing heat-treatment time, due to scattering losses induced by the formation and growth of nanocrystals within the glass matrix.

Specifically at 542 nm the emission of Tb^{3+} (a critical region of interest for scintillator detectors), the transparency of the glass ceramics reaches approximately 65 % for a 2 mm thickness sample following 6 h of heat treatment (top of Fig. 6). The noteworthy transparency of our glass ceramics is a valuable characteristic that enhances their practical application.

The XRD patterns obtained from the powdered glass-ceramic samples are displayed in Fig. 7. Initially, for the NPGF_1 Tb glass, the XRD pattern exhibited two broad peaks with maxima at $2\theta = 27°$ and 45°, characteristic of an amorphous state. However, progressively with the increase of the duration of the heat treatment, four distinct peaks developed at 28°, 32°, 46°, and 54°. These four peaks can be accurately attributed to the pure cubic $Na_5Gd_9F_{32}$ phase (JCPDF 27–0698), evidencing the successful growth of this nanocrystalline phase in the glass matrix after the heat-treatment process.

Transmission electron microscopy (TEM) images were acquired to provide a direct observation of the nanocrystals revealed by XRD results. TEM not only allows distinguishing the crystalline phase from the vitreous matrix but also enables the identification and precise characterization of individual nanocrystals, *e.g.*, their lattice parameters. In the

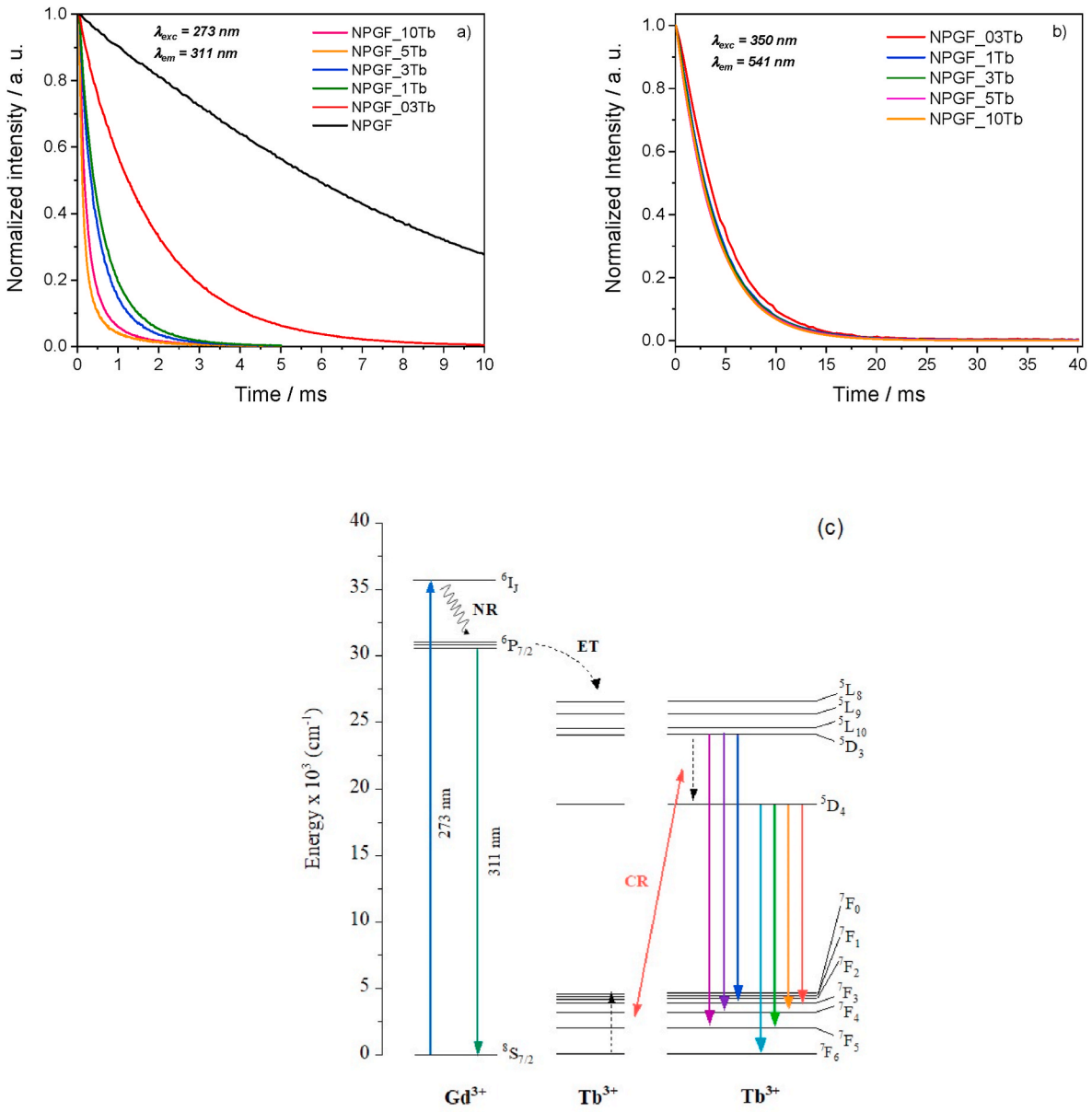

Fig. 4. Decay curves of (a) the Gd^{3+}: $^8S_{3/2} \rightarrow {}^6P_{7/2}$ emission, (b) The Tb^{3+}:$^5D_4 \rightarrow {}^7F_5$ emission of Tb^{3+}-doped NPGF glasses and (c) Partial energy level diagram showing the possible energy transfer from Gd^{3+} to Tb^{3+} ions and emission transitions with cross relaxation (CR) channels in NPGF glasses under 273 nm excitation.

TEM bright-field micrograph, nanocrystals dispersed within the glass matrix can be observed (Fig. 8a) for the sample subjected to heat treatment at 340 °C for 6 h. Moreover, the image in Fig. 8b clearly displays lattice fringes from nanocrystals. The calculated interplanar distance d between two adjacent crystal planes measures 0.325 nm in agreement with the (111) crystal plane of $Na_5Gd_9F_{32}$ where d(111) is reported as 0.321 nm [56].

The influence of the heat-treatment duration and of the formation of cubic $Na_5Gd_9F_{32}$ nanocrystals on the luminescence of Tb^{3+} ions was investigated. The emission spectra of NPGF_1 Tb^{3+} glass and the corresponding glass-ceramics heat-treatment for different times, excited at 350 nm (Tb^{3+}: $^7F_6 \rightarrow {}^5H_7$), are illustrated in Fig. 9. Emission bands originating from the $^5D_4$ and $^5D_3$ excited levels of Tb^{3+} ions are observed at 412, 435, 456, and 472 nm (Tb^{3+}: $^5D_3 \rightarrow {}^7F_5$, $^7F_4$, $^7F_3$, $^7F_2$ transitions), as well as at 489 and 544 nm (Tb^{3+}: $^5D_4 \rightarrow {}^7F_6$, $^7F_5$ transitions). Notably, there is an augmentation in emission intensities obtained for increasing heat-treatment time. However, although there is clearly a trend, conclusions based on the comparison of luminescence intensity are not strict due to the lack of calibrated intensity scale and variable sample positioning. To evaluate a possible change in luminescence efficiency, the quantum yield (QY) of the NPGF_1 Tb and GC_6 h samples (displaying the most intense emission) was measured under excitation at 350 nm. The obtained QY values were 25 % and 33 %, respectively, indicating a significant improvement.

The higher QY value after crystallization (GC_6 h) provides further evidence of the beneficial incorporation of Tb^{3+} ions into the fluoride nanocrystals that have lower phonon energy and are expected to be less defective than the matrix effectively reducing non-radiative relaxation processes.

To further validate the influence of $Na_5Gd_9F_{32}$ nanocrystals on Tb^{3+} emission efficiency, we also investigated the effect of heat-treatment time on the luminescence decay time of Tb^{3+}: $^5D_4 \rightarrow {}^7F_5$ emission at 541 nm (Fig. 10a) and the Gd^{3+}: $^8S_{3/2} \rightarrow {}^6P_{7/2}$ at 311 nm (Fig. 10b) transitions. The decay curves of both transitions exhibited an increase in the lifetime. This finding suggests that Tb^{3+} is influenced by the presence of nanocrystals, effectively reducing non-radiative relaxation

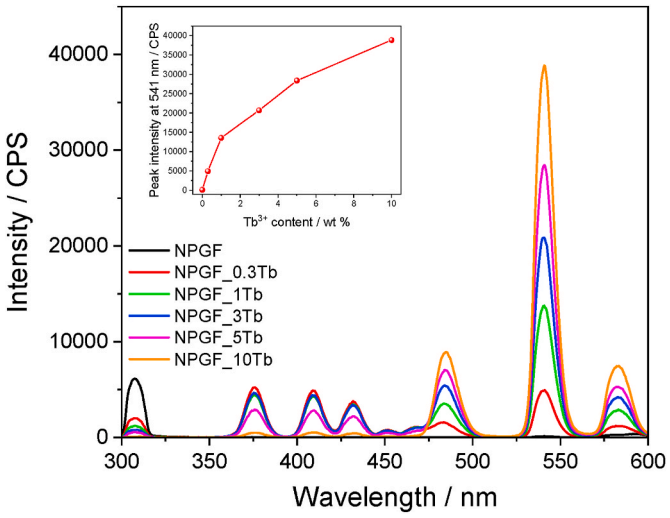

Fig. 5. RL spectra of Tb^{3+} doped NPGF glasses. The inset shows the integrated intensity of the $^5D_4 \rightarrow {}^7F_5$ emission line as a function of Tb^{3+} content.

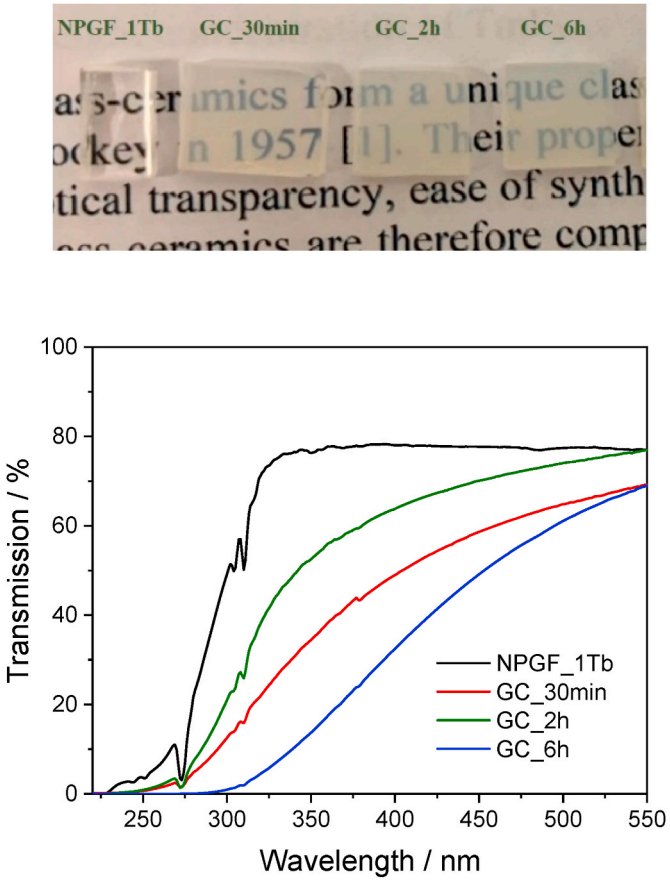

Fig. 6. Top: Photograph of the NPGF_1 Tb glass and derived GCs under ambient light. Bottom: Transmission spectra for NPGF_1 Tb and glass ceramics treat at 340 °C for different times.

processes, and indicates a higher concentration of Tb^{3+} ions within the crystalline phase. This observation is consistent with the results reported in other studies involving glass-ceramics doped with Tb^{3+} ions [34,57,58]. Furthermore, the prolonged decay time of the Gd^{3+}: $^6P_{7/2}$ level with the increase of heat-treatment time agrees with the formation of the Gd-rich crystalline phase $Na_5Gd_9F_{32}$.

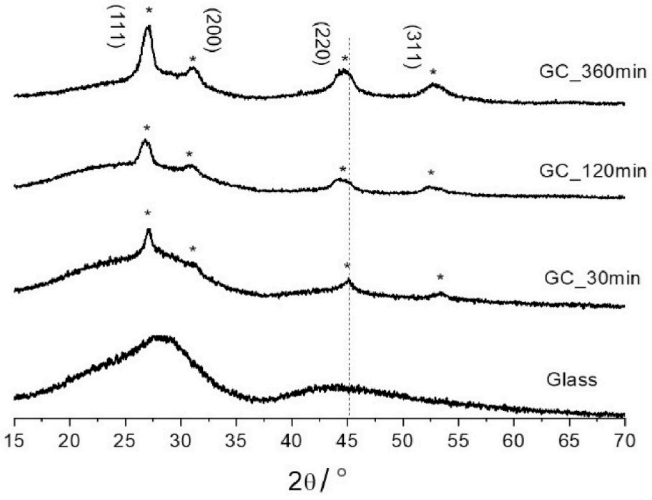

Fig. 7. XRD patterns of NPGF_1 Tb glass and GCs heat-treated at 340 °C for different times, along with the standard X-ray diffraction data for $Na_5Gd_9F_{32}$ (JCPDF 27–0698).

The X-ray induced scintillation spectra of the glass ceramics are presented in Fig. 11. Similarly, to the Tb-doped glasses, these spectra are predominantly characterized by the green emission of Tb^{3+} (Tb^{3+}:$^5D_4 \rightarrow {}^7F_5$). Notably, there is an increase in the emission intensity with an increase in heat-treatment time. The glass ceramic treated at 340 °C for 6 h, the longest duration employed in this study, exhibited the highest scintillation intensity emission.

To evaluate the scintillation efficiency of GC_1 Tb_6 h glass ceramic, a comparison was made with the commercial BGO crystalline powder. This comparison involved measuring, under identical experimental conditions, and determining the total band area for the GC and for BGO whose spectrum is centered at 520 nm.

Therefore, the integrated scintillation response of the glass ceramic was determined to be approximately 36 % of that of the powdered BGO, underscoring its potential scintillating capabilities. Noteworthy, the glass ceramics can still be further improved for the targeted applications as scintillators. First, fluoride phosphate GCs containing fluoride crystals are still under development with especial note for its high solubility of rare earths. Second, as observed for the glass with 10 wt% of $TbCl_3$, higher luminosity is expected for this GC composition. On the other hand, from a fabrication perspective and compared to conventional oxide glasses that have melting temperatures above 1300 °C, the lower melting temperature of the fluorophosphate glass (850 °C, in our case) is advantageous. Moreover, fluorophosphate GCs have higher solubility of rare-earths and higher quantum yield due to the low phonon environment of rare-earths.

4. Conclusions

Fluorophosphate glasses with excellent optical properties were produced using the following molar compositions: $50NaPO_3$–$20BaF_2$–$10CaF_2$–$20GdF_3$:x$TbCl_3$, with *x* values of 0, 0.3, 1, 3, 5 and 10 wt%. We investigated the conversion of UV and X-ray photons into visible photons and evaluated the influence of $Na_5Gd_9F_{32}$ nanocrystals containing Tb^{3+} on the emission properties.

For the Tb-doped samples, when excited in the UV region and by X-rays, they exhibited emissions in the visible region (300–525 nm), stemming from the levels $^8S_{3/2}$ of Gd^{3+} and $^5D_3$ and $^5D_4$ of Tb^{3+} ions. Results clearly evidence that energy transfer from the Gd^{3+} ions to the Tb^{3+} ions significantly enhanced Tb^{3+} emission efficiency.

Transparent glass-ceramics were also prepared. The formation of the cubic $Na_5Gd_9F_{32}$ crystalline phase induced by heat treatment at 340 °C with variable crystallization times was verified. The formation of

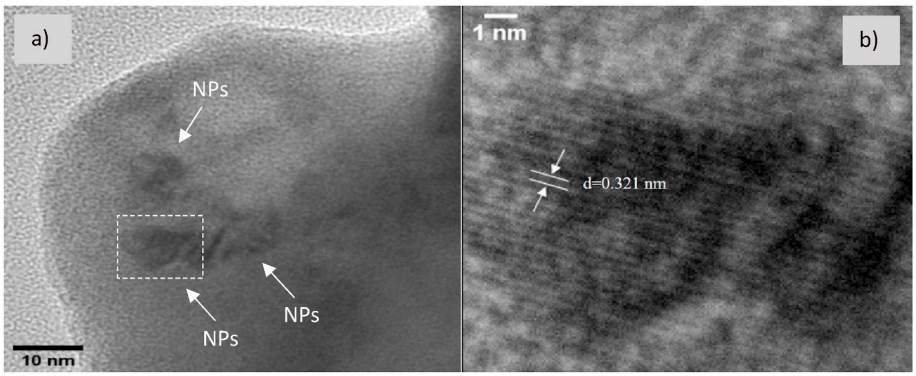

Fig. 8. (a) TEM image of GC_6 h where an area containing nanocrystals is highlighted and (b) HRTEM (High-resolution transmission electron microscopy) image of the crystalline phase.

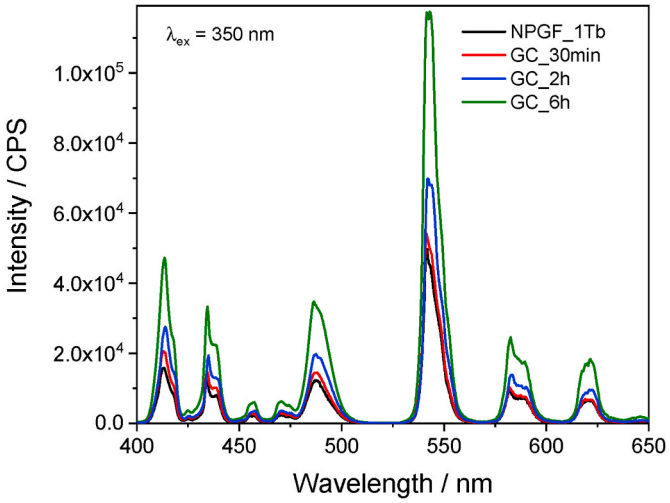

Fig. 9. Photoluminescence emission spectra with excitation at 350 nm (Tb^{3+}: $^7F_6 \rightarrow {}^5H_7$) of NPGF_1 Tb and GCs heat-treated at 340 °C for different times.

crystals led to an amplification of Tb^{3+} ion emission at 542 nm compared to the glass NPGF_1 Tb sample. The increase in intensity, together with the increase in the average lifetime from levels $^8S_{3/2}$ of Gd^{3+} and $^5D_4$ of Tb^{3+} ions, confirmed the incorporation of Tb^{3+} ions in the crystalline environment of $Na_5Gd_9F_{32}$, resulting in an increase in the quantum yield of Tb^{3+} ion emissions from 25 % for the glass samples to 33 % for the GC.

We highlight the fact that the integrated X-ray excited luminescence (RL) intensity of GC_6 h reached 36 % of BGO powder, which is a significant result. Thus, these Tb^{3+}-doped transparent glass ceramics, showcasing high QY, robust RL, and lower melting temperature, as compared to conventional silicate and germate glass ceramics, hold potential for scintillating applications.

CRediT authorship contribution statement

Gustavo Galleani: Conceptualization, Data curation, Formal analysis, Investigation, Methodology, Project administration, Writing – original draft, Writing – review & editing. **Thiago A. Lodi:** Data curation, Formal analysis, Investigation, Writing – original draft, Writing – review & editing. **Robin L. Conner:** Data curation, Investigation. **Luiz G. Jacobsohn:** Data curation, Formal analysis, Funding acquisition, Investigation, Resources, Writing – original draft, Writing – review & editing. **Andrea S.S. de Camargo:** Funding acquisition, Project administration, Supervision, Validation, Writing – original draft, Writing – review & editing.

Declaration of competing interest

The authors declare that they have no known competing financial interests or personal relationships that could have appeared to influence the work reported in this paper.

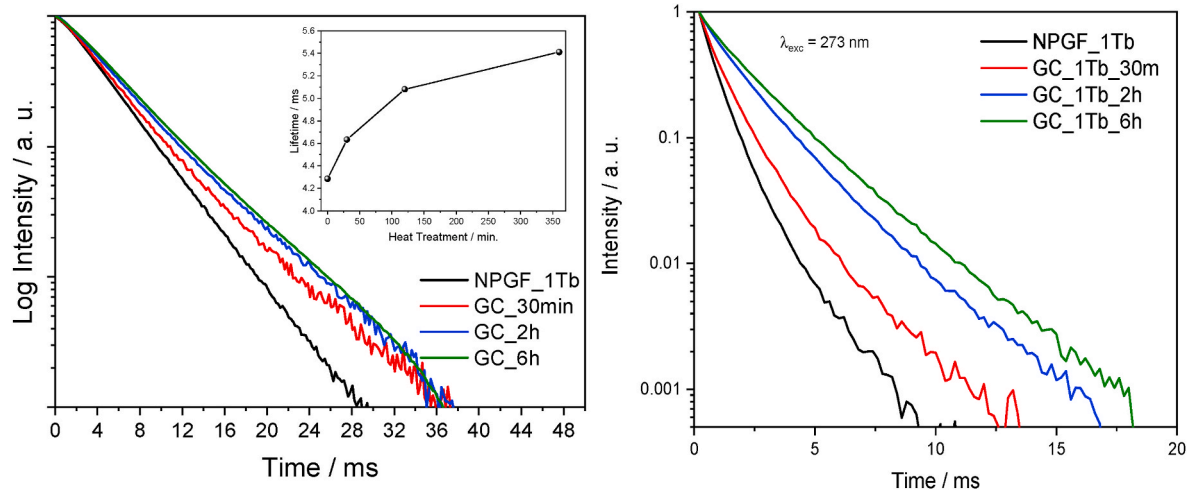

Fig. 10. Decay curves of (a) the Tb^{3+}:$^5D_4 \rightarrow {}^7F_5$ emission and (b) the Gd^{3+}: $^8S_{3/2} \rightarrow {}^6P_{7/2}$ emission of NPGF_1 Tb and GCs heat-treated at 340 °C for different times. The inset shows the average lifetime as a function of heat-treatment time.

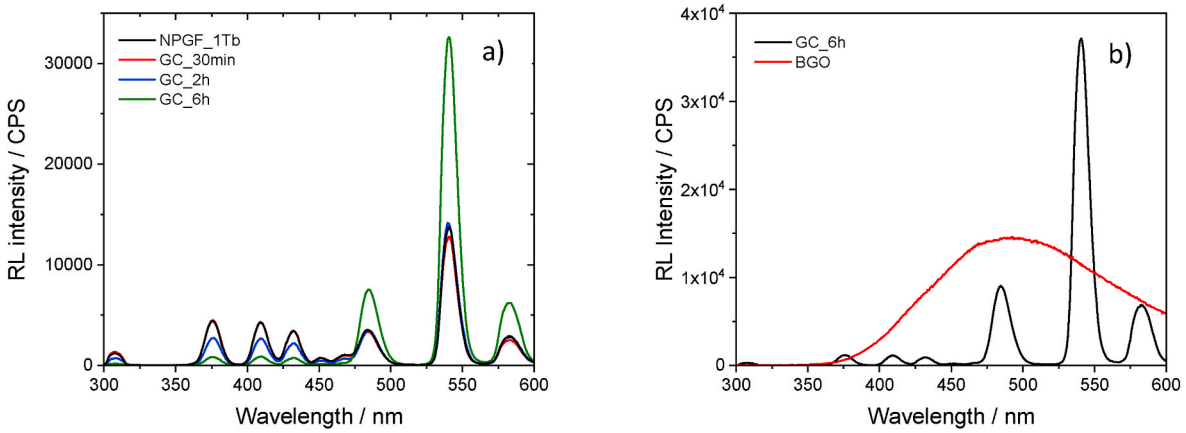

Fig. 11. (a) RL spectra of NPGF_1 Tb and GCs heat-treated at 340 °C for different times. (b) Comparison between RL spectrum of GC_6 h and BGO powder.

Data availability

Data will be made available on request.

Acknowledgments

Authors would like to acknowledge the Brazilian funding agencies FAPESP - Fundação de Amparo à Pesquisa do Estado de SãoPaulo (Project N. 2013/07793-6, CEPID program); CAPES - Coordenação de Aperfeiçoamento de Pessoal de Nível Superior; CNPq - Conselho Nacional de Desenvolvimento Científico e Tecnológico (Universal project 130562/2018-1) and GG acknowledges funding by FAPESP, (Postdoctoral grant number 2018/03931-9). L.G. Jacobsohn's and R.L. Conner's contribution was supported by the National Science Foundation under Grant No. DMR-1653016.

References

[1] Y. Zhou, J. Chen, O.M. Bakr, O.F. Mohammed, Metal halide perovskites for X-ray imaging scintillators and detectors, ACS Energy Lett. Am. Chem. Soc. February 12 (2021) 739–768, https://doi.org/10.1021/acsenergylett.0c02430.

[2] V.B. Mikhailik, V. Kapustyanyk, V. Tsybulskyi, V. Rudyk, H. Kraus, Luminescence and scintillation properties of CsI: a potential cryogenic scintillator, Phys. Status Solidi B 252 (4) (2015), https://doi.org/10.1002/pssb.201451464.

[3] J. Li, J. Ding, X. Huang, Rare earth doped Gd_2O_2S scintillation ceramics, Wuji Cailiao Xuebao/J. Inorg. Mater. (2021), https://doi.org/10.15541/jim20200544.

[4] R. Nicolini, F. Camera, N. Blasi, S. Brambilla, R. Bassini, C. Boiano, A. Bracco, F.C. L. Crespi, O. Wieland, G. Benzoni, S. Leoni, B. Million, D. Montanari, A. Zalite, Investigation of the properties of a 1″×1″ $LaBr_3$:Ce scintillator, Nucl. Instrum. Methods Phys. Res. 582 (2) (2007), https://doi.org/10.1016/j.nima.2007.08.221.

[5] K. Kamada, M. Nikl, S. Kurosawa, A. Beitlerova, A. Nagura, Y. Shoji, J. Pejchal, Y. Ohashi, Y. Yokota, A. Yoshikawa, Growth and scintillation properties of Li and Ce Co-doped $Lu_3Al_5O_{12}$ scintillator, J. Cryst. Growth 452 (2016), https://doi.org/10.1016/j.jcrysgro.2016.04.036.

[6] D.S. McGregor, Materials for gamma-ray spectrometers: inorganic scintillators, in: Annual Review of Materials Research, 2018, https://doi.org/10.1146/annurev-matsci-070616-124247.

[7] M.J. Weber, R.R. Monchamp, Luminescence of $Bi_4Ge_3O_{12}$: spectral and decay properties, J. Appl. Phys. 44 (12) (1973), https://doi.org/10.1063/1.1662183.

[8] T. Yanagida, H. Takahashi, T. Ito, D. Kasama, T. Enoto, M. Sato, S. Hirakuri, M. Kokubun, K. Makishima, T. Yanagitani, H. Yagi, T. Shigeta, T. Ito, Evaluation of properties of YAG (Ce) ceramic scintillators, IEEE Trans. Nucl. Sci. 52 (5 III) (2005), https://doi.org/10.1109/TNS.2005.856757.

[9] M.G. Chapman, M.R. Marchewka, S.A. Roberts, J.M. Schmitt, C. McMillen, C. J. Kucera, T.A. Devol, J. Ballato, L.G. Jacobsohn, Luminescence and scintillation enhancement of $Y2O_3$:Tm transparent ceramic through post-fabrication thermal processing, J. Lumin. 165 (2015) 56–61, https://doi.org/10.1016/j.jlumin.2015.03.041.

[10] Y. Shao, R.L. Conner, N.R.S. Souza, R.S. Silva, L.G. Jacobsohn, Fabrication of ceramic scintillators by laser sintering: the case of $Lu_3Al_5O_{12}$:Pr, Jpn. J. Appl. Phys. 62 (2023), 010601, https://doi.org/10.35848/1347-4065/ac9941.

[11] S.C. Lü, S.F. Zhou, J.Z. Tang, P. Liu, Research progress in development of glass scintillator, Guangzi Xuebao/Acta Photonica Sin. (2019), https://doi.org/10.3788/gzxb20194811.1148011.

[12] T.I. Ratio, T. Lithium, Lithium glass scintillators, Camera 6–7 (1950).

[13] T.A. Lodi, J.F.M. dos Santos, G. Galleani, L.G. Jacobsohn, T. Catunda, A.S.S. de Camargo, Promising Tb_{3+}-doped gallium tungsten-phosphate glass scintillator: spectroscopy, energy transfer and UV/X-Ray sensing, J. Alloys Compd. 904 (2022), 164016, https://doi.org/10.1016/J.JALLCOM.2022.164016.

[14] J.S. Neal, L.A. Boatner, D. Wisniewski, J.O. Ramey, New rare-earth-activated phosphate glass scintillators, in: Proceedings of SPIE - the International Society for Optical Engineering, vol. 6706, 2007, pp. 1–10, https://doi.org/10.1117/12.734561.

[15] L. Pan, J.K.M.F. Daguano, N.M. Trindade, M. Cerruti, E.D. Zanotto, L.G. Jacobsohn, Scintillation, luminescence and optical properties of Ce-doped borosilicate glasses, Opt. Mater. 104 (2020), 109847, https://doi.org/10.1016/j.optmat.2020.109847.

[16] J.M. Park, D.H. Ha, S. Kaewjeang, U. Maghanemi, S. Kothan, J. Kaewkhao, H. J. Kim, Luminescence properties of Ce^{3+} doped gadolinium-calcium-silicaborate glass scintillator, Radiat. Meas. 2016 (2015), https://doi.org/10.1016/j.radmeas.2015.12.028.

[17] X.Y. Sun, Z.H. Xiao, Y.T. Wu, Z. Kang, Fast Ce^{3+}-activated borosilicate glass scintillators prepared in air atmosphere, Ceram. Int. 43 (3) (2017) 3401–3404, https://doi.org/10.1016/j.ceramint.2016.11.187.

[18] Y. Fujimoto, T. Yanagida, S. Wakahara, S. Suzuki, S. Kurosawa, A. Yoshikawa, Luminescence properties and radiation response of sodium borate glasses scintillators, Radiat. Meas. 55 (2013) 124–127, https://doi.org/10.1016/j.radmeas.2013.01.017.

[19] L.G. Jacobsohn, K.B. Sprinkle, C.J. Kucera, T.L. James, S.A. Roberts, H. Qian, E. G. Yukihara, T.A. Devol, J. Ballato, Synthesis, luminescence and scintillation of rare earth doped lanthanum fluoride nanoparticles, Opt. Mater. 33 (2010) 136–140, https://doi.org/10.1016/j.optmat.2010.07.025.

[20] L.G. Jacobsohn, C.L. McPherson, K.B. Sprinkle, E.G. Yukihara, T.A. Devol, J. Ballato, Scintillation of rare earth doped fluoride nanoparticles, Appl. Phys. Lett. 99 (2011), 113111, https://doi.org/10.1063/1.3638484.

[21] M. Koshimizu, Recent progress of organic scintillators, Jpn. J. Appl. Phys. (2023), https://doi.org/10.35848/1347-4065/ac94fe.

[22] W. Chewpraditkul, X. He, D. Chen, Y. Shen, Q. Sheng, B. Yu, M. Nikl, R. Kucerkova, A. Beitlerova, C. Wanarak, A. Phunpueok, Luminescence and scintillation of Ce^{3+}-doped oxide glass with high Gd_2O_3 concentration, Phys. Status Solidi (A) Appl. Mater. Sci. 208 (12) (2011), https://doi.org/10.1002/pssa.201127365.

[23] C. Struebing, G. Lee, B. Wagner, Z. Kang, Synthesis and luminescence properties of Tb doped $LaBGeO_5$ and $GdBGeO_5$ glass scintillators, J. Alloys Compd. 686 (2016), https://doi.org/10.1016/j.jallcom.2016.05.300.

[24] J. Fu, M. Kobayashi, S. Sugimoto, J.M. Parker, Eu^{3+}-Activated heavy scintillating glasses, Mater. Res. Bull. 43 (6) (2008) 1502–1508, https://doi.org/10.1016/j.materresbull.2007.06.024.

[25] J.D. Musgraves, J. Hu, L. Calvez, Handbook of Glass, First edit., 2019.

[26] M.B. Beckert, S. Gallego, Y. Ding, E. Elder, J.H. Nadler, Medical imaging scintillators from glass-ceramics using mixed rare-earth halides, Opt. Mater. 60 (2016) 513–520, https://doi.org/10.1016/j.optmat.2016.09.015.

[27] M.B. Beckert, S. Gallego, E. Elder, J. Nadler, Transitioning glass-ceramic scintillators for diagnostic x-ray imaging from the laboratory to commercial scale, in: Radiation Detectors: Systems and Applications XVII, 2016, https://doi.org/10.1117/12.2249178.

[28] J.K. Cao, X.Y. Wang, X.M. Li, Y. Le Wei, L.P. Chen, H. Guo, Enhanced emissions in Tb^{3+}-doped oxyfluoride scintillating glass ceramics containing KLu_2F_7 nanocrystals, J. Lumin. 170 (2015) 207–211, https://doi.org/10.1016/j.jlumin.2015.10.049.

[29] J. Cao, W. Chen, L. Chen, X. Sun, H. Guo, Synthesis and characterization of $BaLuF_5$: Tb^{3+} oxyfluoride glass ceramics as nanocomposite scintillator for X-ray imaging, Ceram. Int. 42 (15) (2016) 17834–17838, https://doi.org/10.1016/j.ceramint.2016.08.114.

[30] L.A. Boatner, J.O. Ramey, J.A. Kolopus, J.S. Neal, Divalent europium doped and un-doped calcium iodide scintillators: scintillator characterization and single crystal growth, Nucl. Instrum. Methods Phys. Res. 786 (2015) 23–31, https://doi.org/10.1016/j.nima.2015.02.031.

[31] E.V. Van Loef, C.M. Wilson, N.J. Cherepy, G. Hull, S.A. Payne, W.S. Choong, W. W. Moses, K.S. Shah, Crystal growth and scintillation properties of strontium iodide scintillators, IEEE Trans. Nucl. Sci. 56 (3) (2009) 869–872, https://doi.org/10.1109/TNS.2009.2013947.

[32] Z. Yan, G. Gundiah, G.A. Bizarri, E.C. Samulon, S.E. Derenzo, E.D. Bourret-Courchesne, Eu^{2+}-Activated $BaCl_2$, $BaBr_2$ and BaI_2 scintillators revisited, Nucl. Instrum. Methods Phys. Res. 735 (2014) 83–87, https://doi.org/10.1016/j.nima.2013.09.021.

[33] G. Lee, N. Savage, B. Wagner, Y. Zhang, B. Jacobs, H. Menkara, C. Summers, Z. Kang, Synthesis and luminescence properties of transparent nanocrystalline GdF_3:Tb glass-ceramic scintillator, J. Lumin. 147 (2014) 363–366, https://doi.org/10.1016/j.jlumin.2013.11.073.

[34] W. Chen, J. Cao, F. Hu, R. Wei, L. Chen, X. Sun, H. Guo, Highly efficient $Na_5Gd_9F_{32}$:Tb^{3+} glass ceramic as nanocomposite scintillator for X-ray imaging, Opt. Mater. Express (2018), https://doi.org/10.1364/ome.8.000041.

[35] Q. Wang, S. Ouyang, W. Zhang, B. Yang, Y. Zhang, H. Xia, Luminescent properties of Ce^{3+}-doped transparent oxyfluoride glass ceramics containing $BaGdF_5$ nanocrystals, J. Rare Earths 33 (1) (2015) 13–19, https://doi.org/10.1016/S1002-0721(14)60376-8.

[36] K. Biswas, A.D. Sontakke, K. Annapurna, Synthesis and structural probing of Eu^{3+} doped $BaYF_5$ nano-crystals in transparent oxyfluoride glass-ceramics, Int. J. Appl. Glass Sci. 3 (2) (2012), https://doi.org/10.1111/j.2041-1294.2012.00087.x.

[37] J.K. Cao, W.P. Chen, L.P. Chen, X.Y. Sun, H. Guo, Synthesis and characterization of $BaLuF_5$: Tb^{3+} oxyfluoride glass ceramics as nanocomposite scintillator for X-ray imaging, Ceram. Int. 42 (15) (2016) 17834–17838, https://doi.org/10.1016/j.ceramint.2016.08.114.

[38] G.N. Greaves, S. Sen, Inorganic glasses, glass-forming liquids and amorphizing solids, Adv. Phys. (2007) 1–166, https://doi.org/10.1080/00018730601147426.

[39] M. de O. Jr, G. Galleani, C.J. Magon, H. Eckert, Modern magnetic resonance approaches for characterizing rare-earth containing glasses and glass ceramics, J. Non-Cryst. Solids 552 (2021), 120438, https://doi.org/10.1016/J.JNONCRYSOL.2020.120438.

[40] H. Bradtmüller, L. Zhang, C.C. De Araujo, H. Eckert, D. Möncke, D. Ehrt, Structural studies of $NaPO_3$-AlF_3 glasses by high-resolution double-resonance nuclear magnetic resonance spectroscopy, J. Phys. Chem. C 122 (37) (2018) 21579–21588, https://doi.org/10.1021/acs.jpcc.8b06162.

[41] G. Galleani, C. Doerenkamp, S. Santagneli, C. José Magon, S.S. de Camargo A, H. Eckert, Compositional optimization of emission properties for rare-earth doped fluoride phosphate glasses: structural investigations via NMR, EPR, and optical spectroscopies, J. Phys. Chem. C 123 (51) (2019) 31219–31231, https://doi.org/10.1021/acs.jpcc.9b10851.

[42] P.P. Fedorov, A.A. Luginina, A.I. Popov, Transparent oxyfluoride glass ceramics, in: Journal of Fluorine Chemistry, Elsevier B.V., 2015, pp. 22–50, https://doi.org/10.1016/j.jfluchem.2015.01.009.

[43] I. Kawamura, H. Kawamoto, Y. Fujimoto, M. Koshimizu, G. Okada, G. Wakabayashi, M. Nogami, K. Hitomi, K. Watanabe, T. Yanagida, T. Yanagida, K. Asai, Neutron detection via thermoluminescence of Tb^{3+}doped Li_2O-Al_2O_3-B_2O_3 glasses, Jpn. J. Appl. Phys. 60 (3) (2021), https://doi.org/10.35848/1347-4065/abdf7d.

[44] G.L. Ademoski, S. Simko, M. Teeple, I. Morrow, P. Kralik, C.J. Wilkinson, G. Varney, M. Martinez-Szewczyk, L. Yinong, J.K. Nimmagadda, S. Samant, Y. Wu, L. Pan, L.G. Jacobsohn, Q. Wilkinson, F. Duru, U. Akgun, A glass neutron detector with machine learning capabilities, J. Instrum. 14 (6) (2019) P06013, https://doi.org/10.1088/1748-0221/14/06/P06013.

[45] G. Galleani, T.A. Lodi, V.R. Mastelaro, L.G. Jacobsohn, A.S.S. de Camargo, Photoluminescence and X-ray induced scintillation in Gd^{3+}-modified fluorophosphate glasses doped with Ce^{3+}, Opt. Mater. 133 (August) (2022), 112934 https://doi.org/10.1016/j.optmat.2022.112934.

[46] G. Galleani, A.A. Khalil, L. Canioni, M. Dussauze, E. Fargin, T. Cardinal, A.S.S. de Camargo, Fluorine and sodium depletion followed by refractive index modification imprinted on fluorophosphate glass surface by thermal poling, J. Non-Cryst. Solids (2023) 601, https://doi.org/10.1016/j.jnoncrysol.2022.122054.

[47] X. Qiao, H.J. Seo, Vacuum ultraviolet and ultraviolet (VUV-UV) spectroscopy and relaxation dynamics of Eu^{3+} ions doped in $Ca_3Gd_2(BO_3)_4$ phosphor, Mater. Res. Bull. 49 (1) (2014), https://doi.org/10.1016/j.materresbull.2013.08.014.

[48] E. Sarantopoulou, A.C. Cefalas, M.A. Dubinskii, VUV and UV Fluorescence and Absorption Studies of Tb and Tm Trivalent Ions in LiYF4 Single Crystal Hosts, vol. 2007, July 2011, pp. 37–41, https://doi.org/10.1080/09500349414550781.

[49] H. Zhiran, G. Blasse, Energy transfer phenomena in luminescent materials based on GdB_3O_6, Mater. Chem. Phys. 12 (3) (1985), https://doi.org/10.1016/0254-0584(85)90096-3.

[50] R.T. Wegh, H. Donker, E.V.D. Van Loef, K.D. Oskam, A. Meijerink, Quantum cutting through downconversion in rare-earth compounds, J. Lumin. 87 (2000), https://doi.org/10.1016/S0022-2313(99)00514-1.

[51] Y.C. Li, Y.H. Chang, Y.S. Chang, Y.J. Lin, C.H. Laing, Luminescence and energy transferrjproperties of Gd^{3+} and Tb^{3+} in LaAlGe2Q7, J. Phys. Chem. C 111 (28) (2007), https://doi.org/10.1021/jp0719107.

[52] D.J. Robbins, B. Cockayne, B. Lent, J.L. Glasper, The mechanism of $^5D_3$-$^5D_4$ cross-relaxation in $Y_3Al_5O_{12}$: Tb^{3+}, Solid State Commun. 20 (7) (1976) https://doi.org/10.1016/0038-1098(76)90743-2.

[53] C.R. Kesavulu, A.C. Almeida Silva, M.R. Dousti, N.O. Dantas, A.S.S. De Camargo, T. Catunda, Concentration effect on the spectroscopic behavior of Tb^{3+} ions in zinc phosphate glasses, J. Lumin. (2015), https://doi.org/10.1016/j.jlumin.2015.04.012.

[54] Z.X. Wen, L.J. Li, W.J. Huang, S.Y.Z. Chen, L. Lei, T. Pang, H. Guo, Effect of Al powder on Tb^{3+}-doped borogermanate glass for X-ray detection, J. Lumin. (2022) 250, https://doi.org/10.1016/j.jlumin.2022.119095.

[55] L.M. Teng, W.N. Zhang, W.P. Chen, J.K. Cao, X.Y. Sun, H. Guo, Highly efficient luminescence in bulk transparent Sr_2GdF_7:Tb^{3+} glass ceramic for potential X-ray detection, Ceram. Int. 46 (8) (2020), https://doi.org/10.1016/j.ceramint.2020.01.079.

[56] J. Xu, S. Gai, P. Ma, Y. Dai, G. Yang, F. He, P. Yang, Gadolinium fluoride mesoporous microspheres: controllable synthesis, materials and biological properties, J. Mater. Chem. B 2 (13) (2014), https://doi.org/10.1039/c3tb21465f.

[57] Z. Pan, K. James, Y. Cui, A. Burger, N. Cherepy, S.A. Payne, R. Mu, S.H. Morgan, Terbium-activated lithium-lanthanum-aluminosilicate oxyfluoride scintillating glass and glass-ceramic, Nucl. Instrum. Methods Phys. Res. 594 (2) (2008), https://doi.org/10.1016/j.nima.2008.06.041.

[58] X.Y. Sun, S.M. Huang, Tb^{3+}-Activated SiO_2.Al_2O_3.CaO-CaF_2 oxyfluoride scintillating glass ceramics, Nucl. Instrum. Methods Phys. Res. 621 (1–3) (2010), https://doi.org/10.1016/j.nima.2010.04.032.